Monitoring and tracking accessible invariant manifolds in the Cislunar regime

Raymond H. Wright[a], **Luke Tafur**[a], **Naomi Owens Fahrner**[a], **and Joshua Wysack**[a]

[a]*Ball Aerospace*

ABSTRACT

The Cislunar region is becoming an active region of interest for the government, scientific research, and commercial use. With more entities entering the Cislunar regime, Space Situational Awareness (SSA) of this region enables Space Domain Awareness (SDA) to monitor incoming and outgoing threats. It also enables Space Traffic Management (STM) to define safe access to and from Cislunar space. Space mission lifespans are largely driven by consumables, especially for non-electrical propulsion systems. A major consumable is fuel required for launch, orbit insertion, and attitude control. This paper focuses on utilizing the natural bottlenecks that occur from the physics of the three-body problem. These bottlenecks can be used to reduce the search volumes that are exploitable by adversaries using low-cost trajectories. For a satellite to traverse between the Earth and the Moon, such as in the Apollo missions, a satellite needs to have enough energy to open these bottlenecks, thus allowing travel between the two points. This relationship can be used to monitor traffic through the gateway between the Earth and Moon. Using these manifolds, low-cost trajectories that cross this gateway can be found. A plane can then be defined in space that would be capable of monitoring a majority of these trajectories of interest, creating a simpler approach than monitoring the full Cislunar volume. The results show that there exist locations to monitor that result in discovering over 80% of traffic. Work from Klonowski [1] was used to construct optimized Cislunar architectures for these reduced Cislunar volumes of interest. This showed that full observability for the reduced volumes can be achieved with far fewer observers than for the full volume of interest.

1. INTRODUCTION

1.1 Background

In the 1890s, Henri Poincaré studied "paths" that connected the Lagrange points together [2], which was further refined by Conley and McGehee in 1968 [3]. They were able to show that there exist stable and unstable manifolds which create "superhighways" that connect the Lagrange Points. They also showed that once a satellite enters a manifold, it will use little to no energy to maintain its course on the manifold until its destination [3]. Entering and exiting a manifold requires sufficient fuel to provide the necessary change in velocity to:

1. Open the desired Lagrange Point

2. Enter the manifold with sufficient velocity

3. Exit the manifold into an orbit with sufficient velocity

The velocity to enter and exit these manifolds can be designed to be very small and no fuel is consumed once on the manifold trajectory.

1.2 Approach/Method

The method used in this paper was to first investigate which periodic orbits of a subset of families (Lyapunov, Halo, and Vertical) created manifolds that intersected a GEO sphere ranging from 1x to 4x. Once this set of manifolds was found, the data was filtered to see if it was possible to reduce the search volume of the NxGEO intersections. The next step was to define a plane in space that these manifolds crossed through at an opportune location (the bottleneck) to see how many of these manifolds were able to be monitored. These search areas/volumes were then combined with Klonowski's work [1] to see how the reduction affected the Cislunar architectures.

1.3 Dynamics

In the circular restricted three-body problem (CR3BP), the Zero Velocity Surfaces (ZVSs) represents a surface where a third body, the satellite, cannot cross. When the satellite reaches this surface, the satellite's velocity in the direction of the surface becomes zero and the satellite "bounces" off the surface. The other unique feature of the ZVS is the Lagrange Points that are typically defined as points in space between two massive bodies where the gravitational attraction is equal and opposite of the third body. The ZVS defines gateways that can be used to "escape" particular positions in space and all CR3BP planetary systems have this relationship. This paper will focus on the Earth-Moon system relationship with an emphasis on L_1 acting as the lunar gateway, but this can also be applied to systems such as Sun-Earth, Sun-Jupiter, and Pluto-Charon as well.

2.   CIRCULAR RESTRICTED THREE BODY PROBLEM

To quickly summarize the CR3BP, three bodies, P_1, P_2, and P_3 are separated by distances $\vec{d}_n$ and $\vec{r}_n$ within an inertial frame. Using Figure 1 as a visualization, the following assumptions are made to form the CR3BP:

1. P_3 mass is infinitesimal relative to P_1 and P_2, implying P_3 will not influence the motion of P_1 and P_2

2. P_1 and P_2 represent an isolated 2-body system with the center of mass located at the Barycenter since P_3 does not influence their paths.

3. P_1 and P_2 traverse circular orbits; without this assumption, this problem would just be the restricted three body problem.
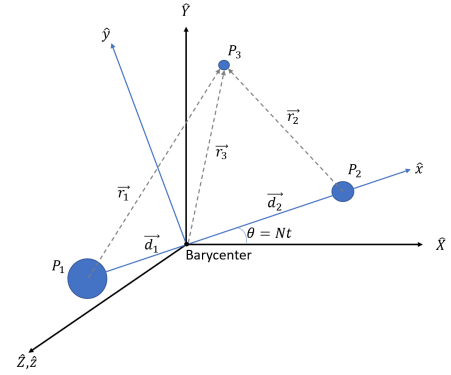

Figure 1: Definition of the CR3BP inertial and rotating frame

2.1 Equations of Motion and Energy

For ease of use, the dimensionless derivations are used for the upcoming derivations with the characteristic values defined in Table 1.

Table 1: Definition of characteristic values

Characteristic Length	$l^* = \vec{d}_1 + \vec{d}_2$
System Mass	$m^* = M_1 + M_2$
Characteristic Time	$t^* = \sqrt{\frac{(l^*)^3}{G(m^*)}}$
Mean Motion for Conic Behavior of Primaries	$N = \frac{1}{t^*}$
Non-dimensional Mean Motion	$n = N \times t^*$
Mass Ratio	$\mu = \frac{M_2}{m^*}$
Non-dimensional time	$\tau = \frac{t}{t^*}$

The equations of motion come directly from Newtons laws of motion and gravitation:

$$M_3\ddot{\vec{r}}_3 = -\frac{GM_3M_1}{|\vec{r}_1|^3}\vec{r}_1 - \frac{GM_3M_2}{|\vec{r}_2|^3}\vec{r}_2 \qquad (1)$$

Using the characteristic values from Table 1 to non-dimensionalize eq. 1; eq. 2 and eq. 3 are broken into its scalar components to create three non-dimensional differential equations (4 - 6) of motions for P_3 under the influences of the larger masses.

$$\frac{\vec{r}_3}{l^*} = \vec{\rho} = x\hat{x} + y\hat{y} + z\hat{z} \qquad (2) \qquad\qquad \dot{\vec{\rho}} = \dot{x}\hat{x} + \dot{y}\hat{y} + \dot{z}\hat{z} \qquad (3)$$

2

$$\ddot{x} - 2n\dot{y} - n^2 x = -\frac{(1-\mu)(x+\mu)}{d^3} - \frac{\mu(x-1+\mu)}{r^3} \tag{4}$$

$$\ddot{y} + 2n\dot{x} - n^2 y = -\frac{(1-\mu)y}{d^3} - \frac{\mu y}{r^3} \tag{5}$$

$$\ddot{z} = -\frac{(1-\mu)z}{d^3} - \frac{\mu z}{r^3} \tag{6}$$

where $d = \sqrt{(x+\mu)^2 + y^2 + z^2}$ and $r = \sqrt{(x-1+\mu)^2 + y^2 + z^2}$ are the derivatives with respect to τ. Completing the derivations requires introducing a new a function similar to the system's potential energy. The "pseudo-potential" function within the rotating frame is defined as follows:

$$U^* = \frac{(1-\mu)}{d} + \frac{\mu}{r} + \frac{1}{2}n^2(x^2 + y^2) \tag{7}$$

Equations 4 through 6 can now be rewritten with respect to eq. 7 resulting in equations 8 through 10.

$$\ddot{x} - 2n\dot{y} = \frac{\delta U^*}{\delta x} \quad (8) \qquad \ddot{y} + 2n\dot{x} = \frac{\delta U^*}{\delta y} \quad (9) \qquad \ddot{z} = \frac{\delta U^*}{\delta z} \quad (10)$$

An important property from eq. 7 and the scalar equations of motion (equations 8 through 10) is the lack of dependence on time. Instead, the equations are dependent on the position of P_3.

2.2 The Jacobi Constant and Lagrange Points

The Jacobi Constant (JC) is an important quantity in the three-body problem. The JC represents an energy-like value of P_3 in the rotating frame. While the conservation of energy is constant for the larger masses, the energy of motion of P_3 is not constant. However, the JC is an integral of motion within the CR3BP that remains constant. Deriving the JC requires taking the dot product of the velocity and acceleration vectors, exploiting the "pseudo-potential" function to write the expression with the partial derivatives of the "pseudo-potential" function.

$$\dot{x}\ddot{x} + \dot{y}\ddot{y} + \dot{z}\ddot{z} = \frac{\delta U^*}{\delta x}\dot{x} + \frac{\delta U^*}{\delta y}\dot{y} + \frac{\delta U^*}{\delta z}\dot{z} \tag{11}$$

Which is equivalent to:

$$\frac{1}{2}\vec{v}^2 = \frac{1}{2}(\dot{x}^2 + \dot{y}^2 + \dot{z}^2) = \int dU^* - \frac{dU^*}{dt} \tag{12}$$

Equation 7 is autonomous allowing $\frac{dU^*}{dt} = 0$. After solving the integral and rearranging the equation, the JC can be written as:

$$C = 2U^* - \vec{v}^2 \quad (13) \qquad C = (x^2 + y^2) + \frac{2(1-\mu)}{d} + \frac{2\mu}{r} - n^2(\dot{x}^2 + \dot{y}^2 + \dot{z}^2) \quad (14)$$

Similar to the "pseudo-potential" function, the Jacobi Constant is autonomous. Given this, at any point in space where both acceleration and velocity vectors of P_3 are 0, P_3 would be stationary at an equilibrium point. There are five well known points called Libration or Lagrange Points $L_i = 1, 2, 3, 4, 5$. Each point in the relative frame is co-planar with P_1 and P_2 at z = 0. The Lagrange Points can be seen in Figure 2 for a μ value of 0.2. Notation-wise going forward, L_1 will be notated as a diamond, L_2 as a square, L_3 as a circle, L_4 as a star, and L_5 as a triangle.
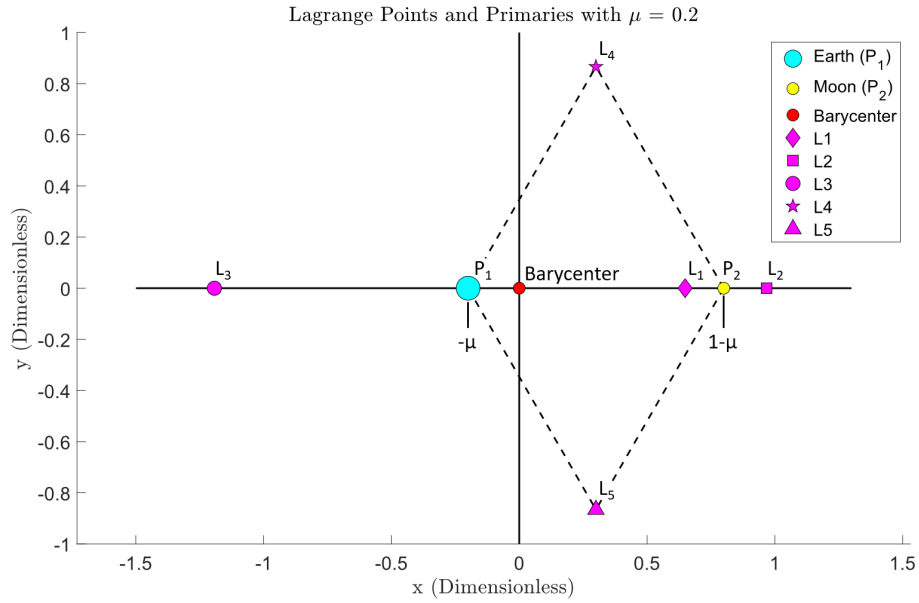
3

Figure 2: Lagrange Points in the CR3BP relative to P_1 and P_2 in the relative frame

2.3 Zero Velocity Surfaces

If one allows P_3 to be at any point in space, $x, y, z \in \mathbb{R}$, and $\vec{v} = 0$, eq. 14 reduces to:

$$C = (x^2 + y^2) + \frac{2(1-\mu)}{d} + \frac{2\mu}{r} \qquad (15)$$

Equation 15 defines the Zero Velocity Surface (ZVS). The ZVS is the transition point where the velocity vector of P_3 transitions from a real number to a complex number mathematically. In terms of actual impacts to the motion of P_3 about P_1 and P_2, the ZVS is a barrier in which P_3 cannot cross. P_3 is able to approach the ZVS, but it will "bounce" off the ZVS when $\dot{\vec{\rho}} = 0$. When the ZVSs intersect with a plane, for example z = 0, Zero Velocity Curves (ZVCs) are formed and can be seen in Figure 3 that demonstrates two unique initial conditions for P_3 with the same JC value. The motion of P_3, the orbit, is confined within the ZVCs. The starting location of P_3 determines if it will orbit P_1 or P_2, but for this case, P_3 cannot traverse between the P_1 and P_2 as the ZVCs forbids this.

Transitioning from 2D to 3D, Figure 4 illustrates two key points, the first being that the surface encloses a volume which bounds P_3 motion. The second is the relationship between the energy-like Jacobi Constant and its effects on P_3. P_3 can move anywhere in the volume defined by the ZVS. As P_3 initial conditions $[\vec{r_3}, \dot{\vec{\rho}}]$ change, then the surface changes as well. In Figure 4, a "smaller" JC corresponds to more energy, expanding the ZVS, allowing access to the Largrange Points, P_1 and P_2.
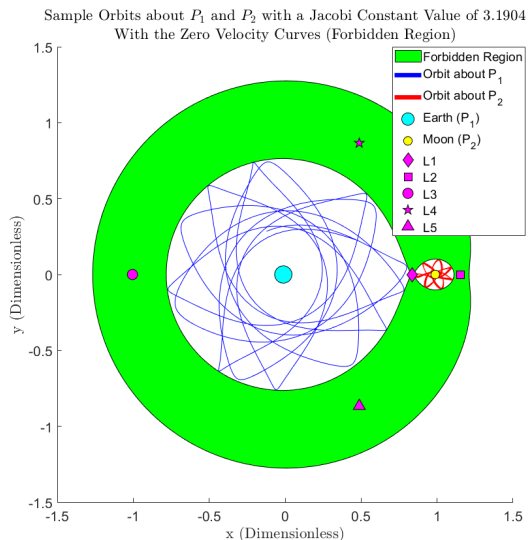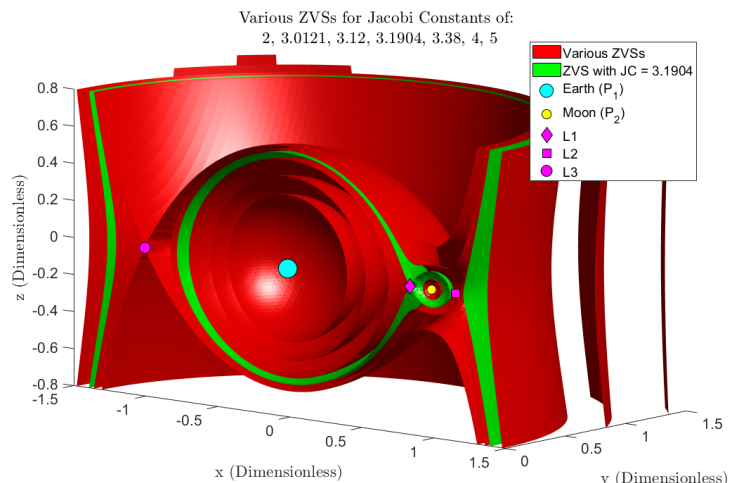
4

Figure 3: ZVCs for JC = 3.1904

Figure 4: Zero Velocity Surfaces with different Jacobi Constant Values
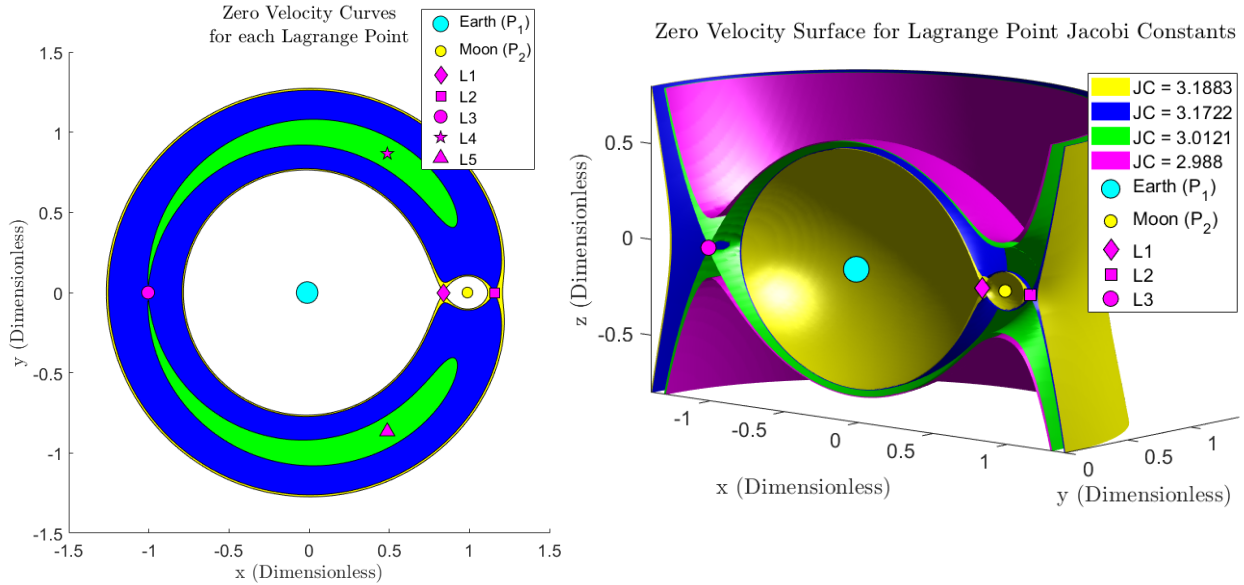
2.4 Lagrange Points

A unique relationship exists between the Lagrange Points, Jacobi Constant, and the ZVS. The Lagrange points act as entry points or doorways between the regions of space surrounding P_1 and P_2 in the CR3BP. To unlock access between P_1 and P_2 for example, Lagrange Point 1 (L_1) needs to be opened. To open L_1, P_3 needs to achieve a JC of 3.1883 or smaller. If P_3 intends to reach L_2, it must satisfy a JC value such that it opens the ZVS at L_1 allowing it to gain access to the moon and open the ZVS at L_2. If P_3 intends to orbit about L_4/L_5, a JC value that opens the ZVS at $L_{1,2,3}$ is needed.

Figures 5a and 5b represent the same zero velocity surfaces. Within the figures are five ZVSs corresponding to five JC values (see Table 2) needed to access (unlock) the Lagrange Points. Figure 5a is a two dimensional slice through the XY-plane at z = 0 of Figure 5b, resulting in ZVCs.

Table 2: Lagrange Point Jacobi Constant values and color relationship to Figure 5

Lagrange Pt	Jacobi Constant	Figure 5 ZVS Color
L_1	3.1883	Yellow
L_2	3.1722	Blue
L_3	3.0121	Green
L_4	2.9880	Magenta
L_5	2.9880	Magenta

Notice in Figure 5a the magenta color does not appear due to the Zero Velocity Curve being sliced at z = 0 where the magenta surface does not intersect. When JC = 2.998, the surface is connected at L_4 and L_5. The surface still exists which can be seen in Figure 5b and the doorway through L_4 and L_5 has opened with unrestricted motion in the XY-plane.

5

(a) Various Zero Velocity Curves associated with the Lagrange Points

(b) The full surface representation of Figure 5a (sliced down the Z-Y plane). The unique colors represent different JC values.

Figure 5: A 2D and 3D slice of various Zero Velocity Surfaces. Figure 5a is the 2D slice in the XY- plane of Figure 5b

Within the Zero Velocity surfaces, Lagrange Points 1, 2, and 3 (L_1, L_2, L_3) can act as gateways between the two massive bodies. L_1 is the gateway from Primary Body 1 (Earth) to Primary Body 2 (Moon), L_2 is the gateway to "escape" the system into space from the Primary Body 2 (Moon) side, and L_3 is the gateway to "escape" the system into space from the Primary Body 1 (Earth) side. These gateways also allow entry into the system.

2.5 Periodic Orbits about L_1 and L_2

A vast amount of research has defined periodic orbits that exist about all of the Lagrange Points in the Earth-Moon system including Lyapunov, Halo, Vertical, Butterfly, etc.[4] and their Planar resonance orbits (1:1, 2:3, 4:2, ...)[4]. This paper will focus on missions between the Earth and L_2 to include the Moon and L_1 between them, which enter Lyapunov, Halo, or Vertical orbits. The methods used can be applied to other periodic orbit families as well.
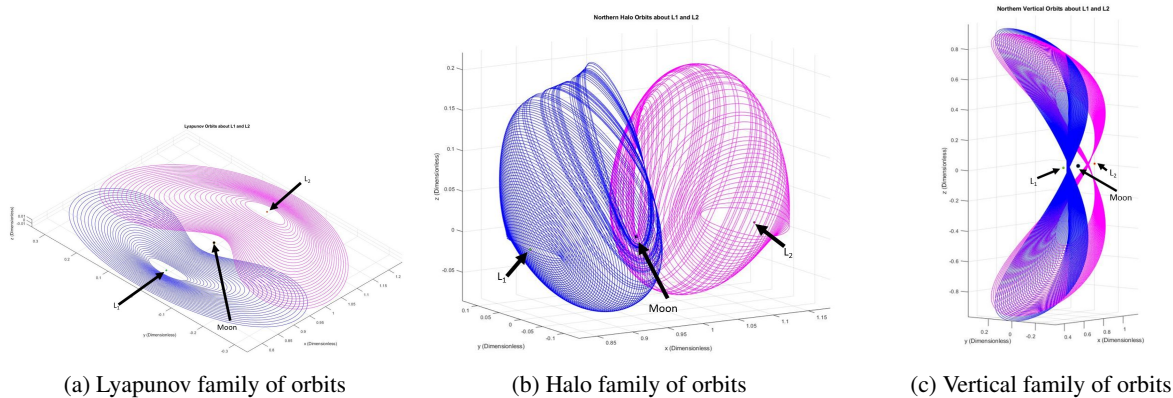

(a) Lyapunov family of orbits

(b) Halo family of orbits

(c) Vertical family of orbits

Figure 6: Examples of various periodic orbits about L_1 and L_2 that are used in this research.

3. INVARIANT ORBITAL MANIFOLDS

3.1 Manifold History

In the 1890's Jules-Henri Poincaré was very interested in the three-body due to its difficulty. He wondered how to solve the dynamic system that required four integrals of motion, but only one existed (eq. 14). He reasoned that if all

6

orbits within a system with a $JC = C_o$, the motion (orbit) may be restricted by a second integral. Each orbit on this "manifold" would lie on a 2-D surface embedded in a 3-D surface. The simple way to examine this surface is to slice it and create a two-dimensional map. Two conditions arise from this Surface of Section approach when the orbit is numerically integrated and plotted:

- A random distribution of points will occur if a second integral of motion does not exist.

- A constrained shape will lie on the surface if a second integral of motion does exist.
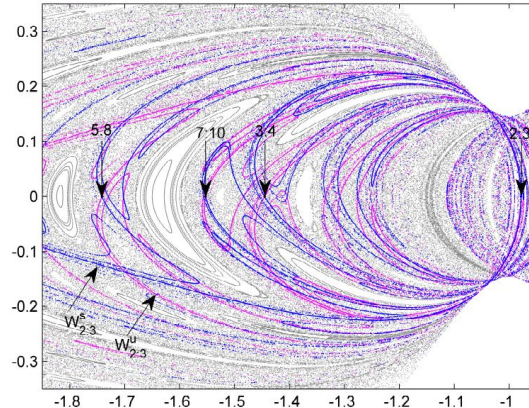
Figure 7: Poincaré Section Illustrating the Relationship between the Invariant Manifolds of the 2:3 Resonant Orbit and Other Resonant Trajectories - Saturn-Titan System[5]

Poincaré found that both behaviors existed at the same time and described this effect in 1892 (illustrated in Figure 7). It was not for another hundred years that the application of this work was realized. During the mission planning for the NASA Genesis mission, Martin Lo, Kathleen Howell, and others devised a way to use these manifolds to traverse the solar system while minimizing delta-Velocity (delta-V)[6]. Figure 7 demonstrates the chaos versus order in a map. Escribano[5] was investigating resonant orbits in the Saturn-Titan system, but these maps exist in every three-body system. Escribano highlights some the constrained shapes that exist in the system studied showing that there exists multiple manifolds that P_3 can traverse within that system. Theoretically, once P_3 enters onto a manifold, it requires no additional fuel to maintain its course until it has reached its final destination.

3.2 Generating Manifolds

These manifolds can be found by using the same method to generate the periodic orbits in Figure 6. Using the periodic orbit as the starting or ending condition, a slight positional and velocity offset is applied. Propagating the orbit forwards or backwards in time will create two unique manifold solutions: an unstable manifold (forward in time), and a stable manifold (backward in time). Using a periodic L_1 Lyapunov orbit, these manifolds can be seen in Figure 8 that show the trajectories are bound within the zero-velocity curves.

Like the periodic orbits themselves, the manifolds are bounded by the ZVS (Figure 9) since the manifolds represent a potential orbit for P_3. The Lyapunov manifolds are bounded in the X-Y plane of the CR3BP. A key observation is that any orbit that enters/leaves via the L_2 gateway is bounded by the ZVS around the moon and L_1. This pinch point at L_1 is an optimal place for an SDA mission that is monitoring incoming and outgoing objects to/from the Moon and L_2. Lines and planes are also shown in these figures at x = 0.5 ($\sim$4.6x GEO) and x = 0.81132 ($\sim$7.5x GEO) that will be further discussed in section 4.3.
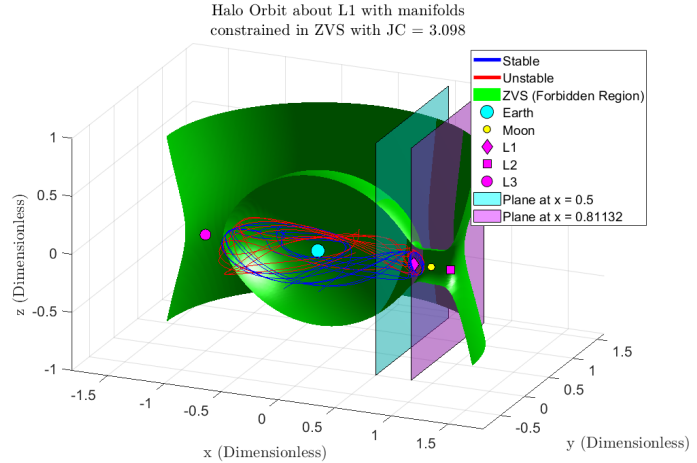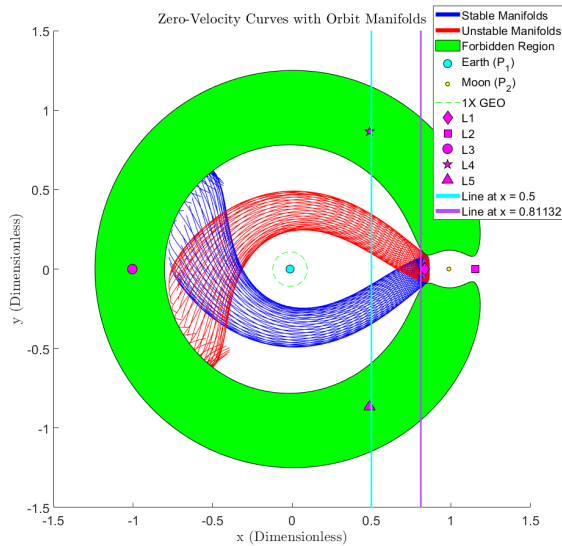
7

Figure 8: A Lyapunov Orbit about L_1 constrained in a Zero Velocity surface with Stable (blue) and Unstable (red) manifolds

Figure 9: Manifolds propagated from/to a periodic L_1 Halo orbit

4. DEFINING AN SDA MISSION

The Space Domain Awareness mission has historically been defined to detect and track artificial objects, especially threat based objects, entering/exiting Earth orbits. The search volume includes the full spherical volume about Earth. The invariant manifolds provide a low-cost delta-V trajectory between Earth, Cislunar corridor, Lunar, and beyond requiring an expansion of the SDA capability to now include detection and tracking of artificial objects beyond the GEO belt. Currently, the community has not settled on the extent of the expansion volume within the Earth-Moon system an SDA mission must address. Some have offered four times the GEO belt (4xGEO), others state ten times (10xGEO), extending past the Moon but ending prior to L_2. This is due to the SDA "trip-wire" being defined at 4xGEO and 10xGEO is the STM volume to keep track of most objects in the Earth-Moon neighborhood. By exploiting these manifolds, the search volume can be reduced to not include the entire spherical volume.

4.1 Propagating the Manifolds

Using the initial conditions provided by NASA JPL [4], a total of 6977 periodic orbits were selected. The 6977 orbits contain three orbital families, Lyapunov, Northern Halo, and Northern Vertical that either orbit L_1 or L_2. The following method was used to propagate the orbits:

1. Propagate one period for each periodic orbit (6,977 unique periodic orbits).

2. Select a position and velocity offset from the periodic orbit that enters both stable and unstable manifolds then propagate. Repeat this process 9 more times, for a total of 10 unique trajectories evenly spaced along the periodic orbit that produces the manifolds. See Figure 10 for examples of the starting locations.

3. Define the maximum propagation time as 41 dimensionless time units (τ from Table 1) which is approximately a half Earth calendar year.

4. Propagate the manifolds until:

   - The manifold crosses at 1x, 2x, 3x, or 4xGEO orbit.
   - Any orbit that does not cross 1x, 2x, 3x, or 4x and is propagated the maximum time will be excluded from the study as it is shown that the manifold will not intersect at the desired GEO radii within the defined time of interest. Depending on the volume of interest and/or the maximum transit time, this could be modified for other missions.
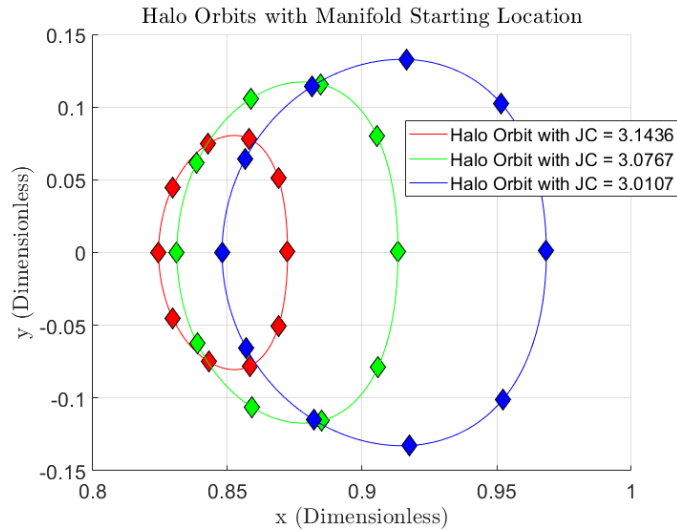
8

Figure 10: Example of various periodic orbits and the starting locations for the stable/unstable manifolds. Each diamond represents a unique starting location of an orbit on the surface of a manifold associated with that periodic orbit.

4.2 Propagation Results

In total, 6,977 unique periodic orbits each with 10 stable and 10 unstable manifolds were investigated - that equates to a total of 139,540 unique trajectories. A total of 62% of the manifold orbits crossed one or more of the GEO radii. Of the orbits that crossed a GEO radii, approximately 47% were on a stable manifold and 53% were on an unstable manifold. Due to the dynamics, trajectories leaving/entering the NxGEO orbit were a mixture of stable and unstable manifolds and those are not directly related based on the approach.

The data is presented using a point cloud to show where an orbit crossed a NxGEO Poincaré-like sphere. Two color schemes are shown to further delineate the data. First, the magenta, blue, green, then red represent a crossing at the 1x, 2x, 3x, and 4xGEO orbits. Then each point is scaled by the delta-V from black being the smallest delta-V, to full color (magenta, blue, green, red) for maximum delta-V. For the Stable manifolds, delta-V represents the delta-V needed to exit the circular orbit about the GEO sphere and enter the manifold which will take P_3 to the periodic orbit at L_1 or L_2. Whereas the delta-V for the unstable manifolds, defines the delta-V needed for P_3 to exit the manifold (which started at the periodic orbit [see Figure 10]) and inject into a circular orbit at that GEO radius. Note, these orbits are not equatorial as that would require another delta-V to change the inclination. Figure 11 shows the unstable L_1 Halo family and these figures were also generated for the other families and for stable/unstable manifolds, but this one was the most interesting. The statistics for the delta-V for the unstable L_1 Halo family can be seen in Table 3 and propagation time can be seen in Table 4. Data was generated for all families investigated, but unstable L_1 Halo is all that is shown.

- First, P_3 is more likely to enter the stable manifold in the -Y regime and exit the unstable manifold in the +Y regime.

- There are fewer GEO crossings for manifolds connecting a GEO sphere and L_2, (67.3% of the crossings were manifolds connecting to L_1). This occurs since the L_2 periodic orbits must either traverse through the L_1 gateway or gain enough energy to go all the way around to the L_3 gateway.

- There are two cases (Unstable Northern Halo L_2 and Stable Northern Vertical L_1) where the manifolds did not cross the 1xGEO sphere.

- Most of the orbits appear to be constrained in the Z-direction, with manifolds between L_1 originating from the Northern Halo family the exception.

- 60% of the crossings were from the Lyapunov family, 38% crossings were Halo, and 2% were from the Vertical family.

9

- 3.5% of the manifolds crossed 1xGEO, 15.5% crossed 2xGEO, 34% crossed 3xGEO, and 47% crossed 4xGEO.

- Larger delta-Vs are needed to enter/exit a smaller (1xGEO) orbit than a larger (4xGEO) orbit

To speak to the figures not shown, Lyapunov L_1 and L_2 orbits, both the stable and unstable intersections, were planar at z = 0 creating concentric rings about each NxGEO belt. The L_1 Halo family were the most filled in resembling intersections almost around the full sphere for the unstable and missing some of the rear intersections (away from the Moon, towards L_3) for the stable intersections. The L_2 Halo orbits had less intersections, being very tightly bound covering about ∼1/8 of the sphere's surface area. The Vertical family had the least amount of intersections with the unstable being more tightly grouped than the stable, but still very sparse in comparison to the other families.

Table 3: delta-V (ΔV) statistics for the unstable L_1 Halo family

GEO Radius	Minimum ΔV [km/s]	Maximum ΔV [km/s]	Average ΔV [km/s]	1 σ ΔV [km/s]
1x	1.0549	4.9716	2.5526	0.9842
2x	0.5378	3.5272	1.4853	0.7192
3x	0.3228	2.8826	1.0278	0.5266
4x	0.1902	2.2107	0.8996	0.4404

Table 4: Time statistics for the unstable L_1 Halo family

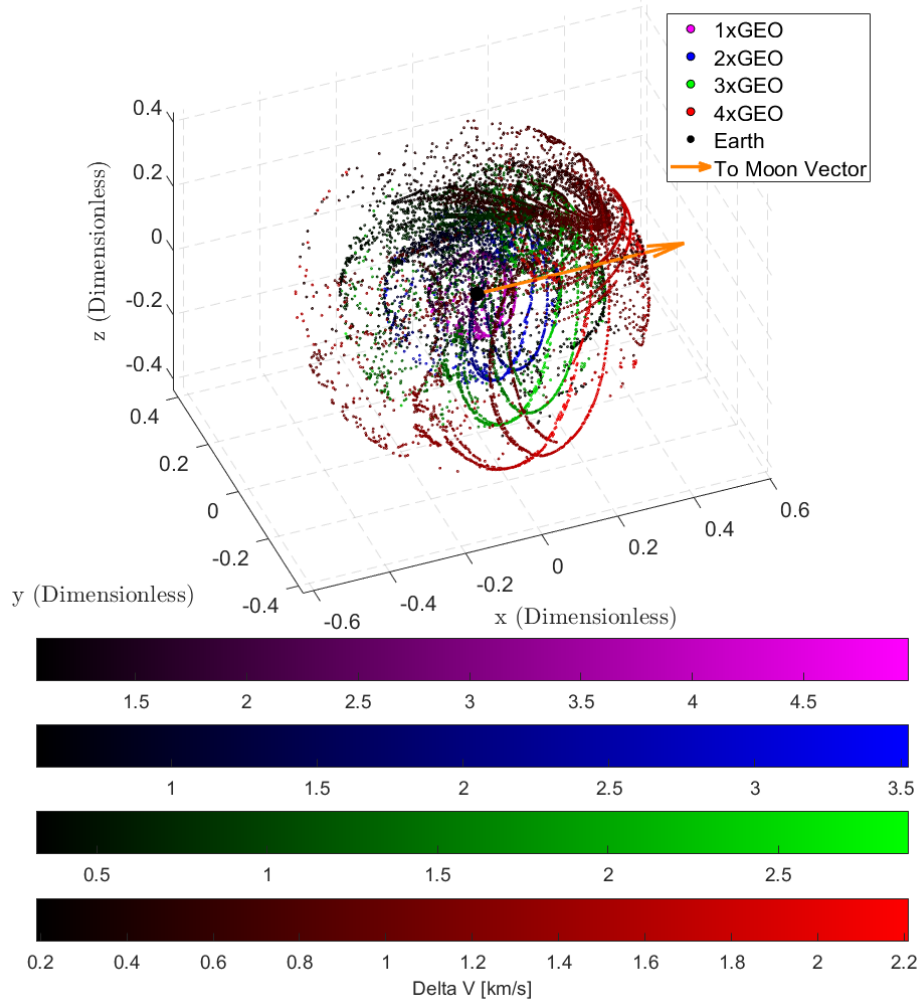| GEO Radius	Minimum Time [days]	Maximum Time [days]	Average Time [days]	1 σ Time [days]
1x	42.2810	181.7233	94.9208	52.6102
2x	29.6552	181.7038	87.1361	47.2322
3x	29.2609	181.7186	71.4650	41.0138
4x	28.6232	181.6786	62.6001	36.6991

Figure 11: Poincaré-like surface for 1x through 4xGEO Unstable crossings for L_1 Halo Family. The color bars define the delta-V needed to insert or exit a particular GEO sphere.

### 4.3 SDA Missions Monitoring a GEO Sphere

4.3.1 Propagation Time and Delta-Velocity Clipping

Defining a reasonable SDA mission to monitor the GEO sphere requires an understanding of the targets, but in lieu of this, the data was filtered down using statistics. Filtering the data by using delta-V and propagation time is used since the longer an object takes to traverse along the trajectory, the higher the probability to detect the object, and the larger the insertion delta-V is, the more unrealistic (especially on the unstable manifold) the mission becomes due to the amount of fuel mass P_3 would need to carry. Two methods of "sigma clipping" occurred where the first method reduced the data by time then delta-V and the second method reduced by delta-V then time. The "sigma clipping" in this case is defined as removing data above the mean plus one standard deviation if the value is to be minimized or removing data below the mean minus one standard deviation if the value is to be maximized.

Any P_3 propagation time that exceeded the average time plus one standard deviation would be removed from the data set. Using the reduced data set, a new average delta-velocity and standard deviation would be calculated. The reduced data set is further reduced by any delta-V that exceeds one mean plus standard deviation of the remaining delta-V (Figures 12a and 12b). Figures 12c and 12d instead, using a similar method, were first clipped by the delta-V, then propagation time.
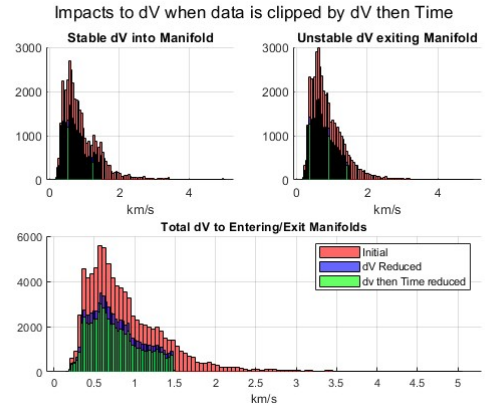
11
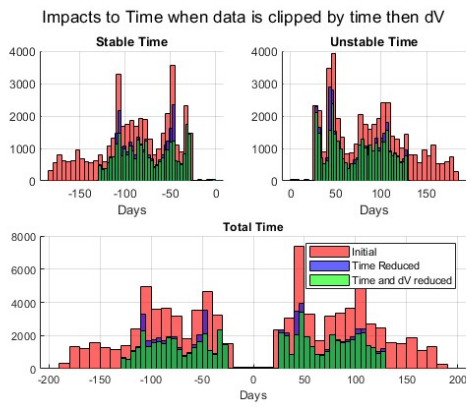
(a) Propagation Time reduced by clipping Time then dV
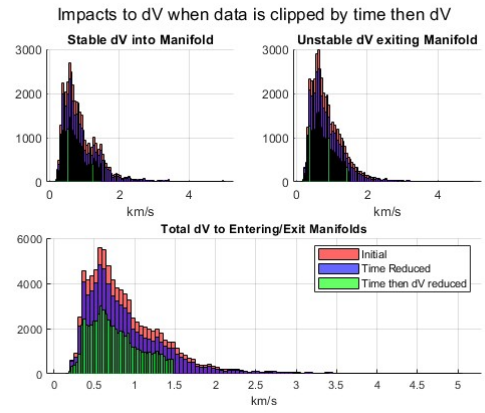
(b) Delta-Velocity reduced by clipping Time then dV
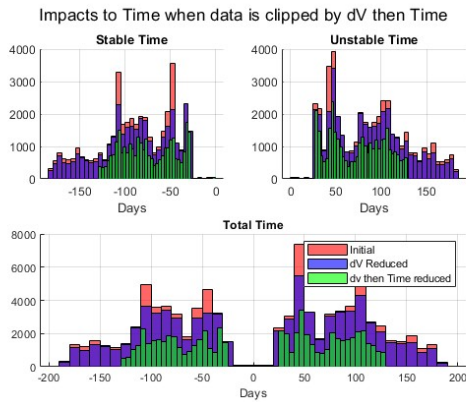
(c) Propagation Time reduced by clipping dV then Time

(d) Delta-Velocity Time reduced by clipping dV then Time

Figure 12: Investigation into reducing the volume by filtering Time and Delta-Velocity by sigma clipping time and delta-V. The Y-Axis represents the total number of orbits that fell within the histogram bin.

Regardless of the clipping order, the reduced data set returned similar results. The original average propagation time of 87.7 +/- 41.4 days was reduced to 73.7 +/- 29.7 days or 74.1 +/- 29.8 days. The delta-Velocity magnitude was reduced from 0.916 +/- 0.558 $\frac{km}{s}$ to 0.762 +/- 0.308 $\frac{km}{s}$ or 0.752 +/- 0.305 $\frac{km}{s}$.
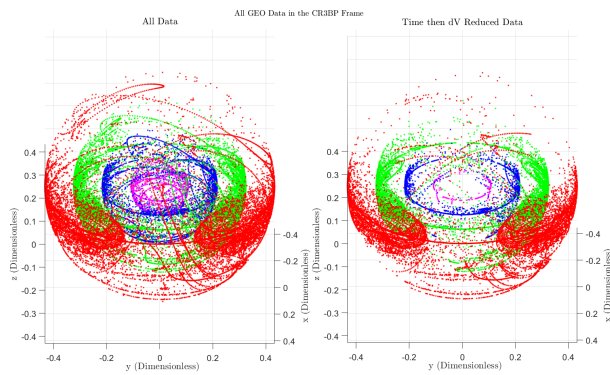
(a) All GEO crossing clipped by Time then dV
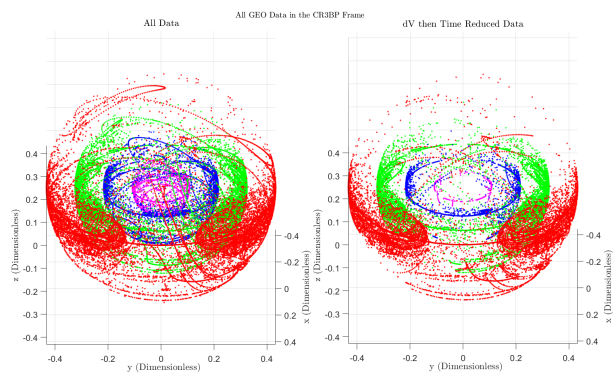
(b) All GEO crossing clipped by dV then Time

Figure 13: All GEO crossing clipped either by time then dV or dV then time on a Poincaré-like GEO surface for each GEO radius

12

Both clipping methods reduced the number of crossings by 27%, allowing an SDA mission to monitor 73% of the activity. Unfortunately the overall search volume has not been reduced and still requires an SDA mission to track the entirety of each GEO sphere since the reduction is just in density and not a particular area.

4.3.2 Position Clipping

In section 4.2, it was noted that most of the orbits were bound by height in the Z-direction. Instead of using time and delta-V as the clipping methods, the height in the Z-direction was used to filter the data set. Any orbit that entered a GEO sphere above or below the Z-threshold was removed to see if that would reduce the overall search volume. While a unique Z-threshold can be applied to each GEO sphere, a standard Z-threshold was applied to all of the GEO spheres (+/- 0.163 dimensionless units (DU), ~1.5xGEO). This was done for two reasons, the first is that any GEO sphere less than 4x MUST pass through the 4x boundary, however an orbit that passes through the 4x boundary may not pass through a lower GEO sphere, see Table 5.

Table 5: Unique Orbital Crossings for Various GEO Orbits (Prior to Z-clipping)

GEO Radius	Total	Stable	Unstable
1x	3068	1487	1581
2x	13383	6225	7158
3x	29414	13867	15547
4x	40728	19300	21428

From the target's (P_3) perspective, entering a circular orbit at 4xGEO requires less delta-V. For example, if P_3 were returning to Earth via an unstable manifold, it could perform a maneuver when it reached 4xGEO to enter a circular orbit about Earth, then at an opportune time, perform another burn to reach a 1xGEO orbit using less delta-V (Figure 14) than if it had selected a direct inject manifold to the 1xGEO sphere. Looking at the results from Table 5, a mission that can track objects entering/exiting the 4xGEO sphere has the capability to detect over 10 times the number of targets than a mission focused on the 1xGEO belt. This means that from a mission perspective, if a mission is designed to a larger NxGEO sphere, then all of the smaller spheres will be captured as well.
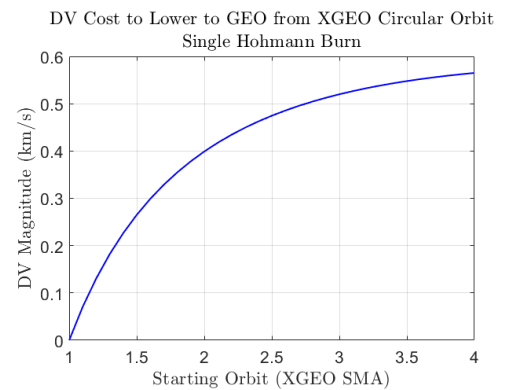

Figure 14: Delta-V needed to change from a larger GEO orbit to 1xGEO using a Hohmann transfer
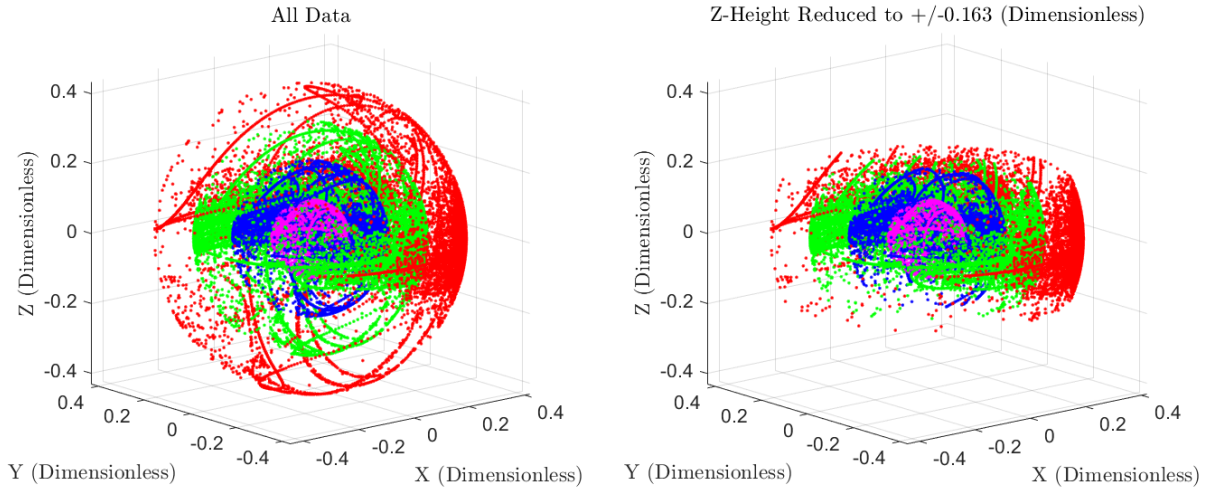
13

Figure 15: Reducing search volume for an SDA mission by constraining the height in the Z-direction.

When the data is clipped in the Z-direction (Figure 15) over 94% of the crossings remain observable, with 95% observability of the stable manifolds and 93% observability for the unstable manifolds. This can be broken down further by family and Lagrange point.

Table 6: Detectable Crossings with a reduction in the Z direction per Family and Lagrange Point. *The volume increase for 1xGEO case

GEO Radius	Lyapunov L_1	Lyapunov L_2	Halo L_1	Halo L_2	Vertical L_1	Vertical L_2	Volume Reduction
1x	100%	100%	100%	100%	100%	100%	N/A*
2x	100%	100%	78.3%	100%	100%	100%	8.3%
3x	100%	100%	75.7%	100%	87.1%	71.6%	31%
4x	100%	100%	68.9%	100%	91.4%	78.6%	46.1%

The Lyapunov orbits are all contained within the X-Y plane and therefore the clipping in the Z direction will have no effect. Manifolds connecting to the Halo periodic orbits about L_1 see the most reduction, followed by all of the Vertical orbits. The Volume Reduction column compares a full NxGEO volume to the volume clipped in the Z-direction +/- 0.163 DU. A useful way to interpret Table 6 is an SDA mission that is designed to monitor the 4xGEO can detect each of those orbital crossings while searching 63.9% of the 4xGEO volume. By using the mean and standard deviation for the height in the Z-direction for all crossings, the searchable volume was larger than the 1xGEO sphere volume. However, an SDA mission that searches GEO spheres larger than 1xGEO see an immediate reduction in the searchable volume using this clipping method. The advantage of this method is the total observability of the manifolds is much higher and the search volume is significantly reduced for larger GEO spheres.

4.4 Preliminary Observability Analysis

A preliminary analysis of the observability pertaining to the clipped volumes was executed using a Multi-Objective Monte Carlo Tree Search algorithm (MO-MCTS). This algorithm generated optimized Cislunar architectures that maximized observability, also referred to as coverage, for volumes of interest. The primary objective of this analysis was to conduct a comparative evaluation of the overall observability achieved by optimized Cislunar architectures for both the clipped volume and the complete 4xGEO sphere. To mitigate any potential bias in the resulting architectures, the MO-MCTS underwent 1000 iterations for each of these volumes, encompassing multiple epochs. For a comprehensive understanding of the methodology adopted, refer to Klonowski's work in [1].

This volume was clipped at z = +/- 0.1631 DU and at 1xGEO, 2xGEO, 3xGEO, 4xGEO belts, as represented in Figure 15. For simulation purposes, each belt was defined with a 0.01 DU width. Observability was quantified by an SNR threshold of 6 using with a 200mm telescope. Additionally, the solar phase angle was considered in this architecture

14

design. As in [1], orbits with 1:1, 1:2, 1:3, 1:4, 2:1, 3:1, 3:2, 4:3, 5:2, 5:3, 5:4, and 6:5 resonance with the synodic period were considered. This includes orbits such as the following:

- L_1 and L_2 Lyapunov, Halo, Axial, and Vertical
- L_4 and L_5 Axial, Planar, and Long
- Distant Retrograde and Prograde, Low Prograde
- 1:2, 1:3, 2:3, 3:2 Resonant Orbits (resonance with the CR3BP period)
- Geo Orbit

The resulting optimized architectures with their associated total observabilities for each of the volumes can be seen in Figures 16 - 18. Note: the astute reader may notice that the "geo" orbits look off-centered from the Earth. This results from these orbits not being perfectly circular, bit slightly ovaled.
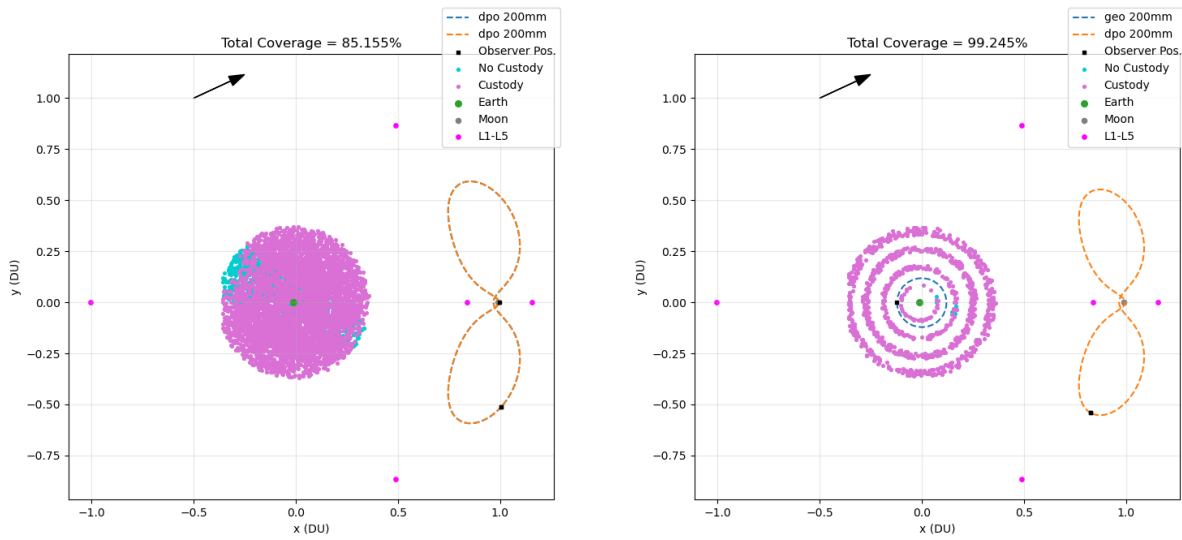
(a) Full 4xGEO Volume   (b) Clipped Volume

Figure 16: Total Coverage of Full Volume vs. Clipped Volume with 2 Observers
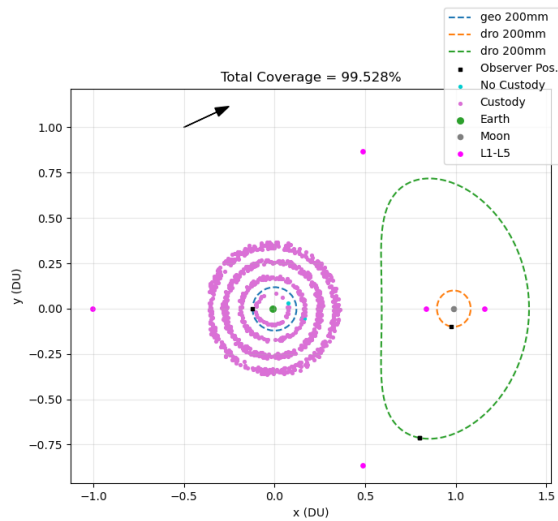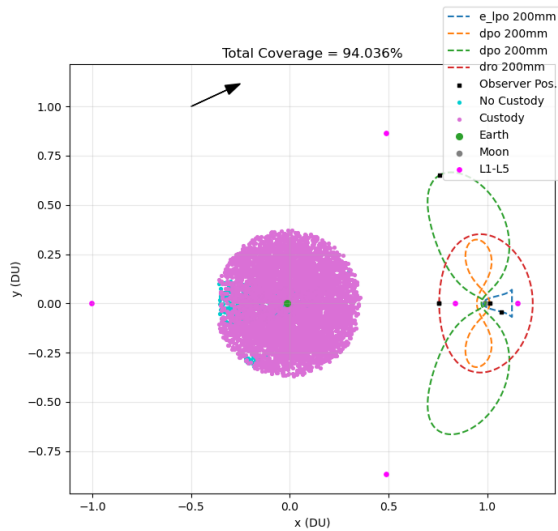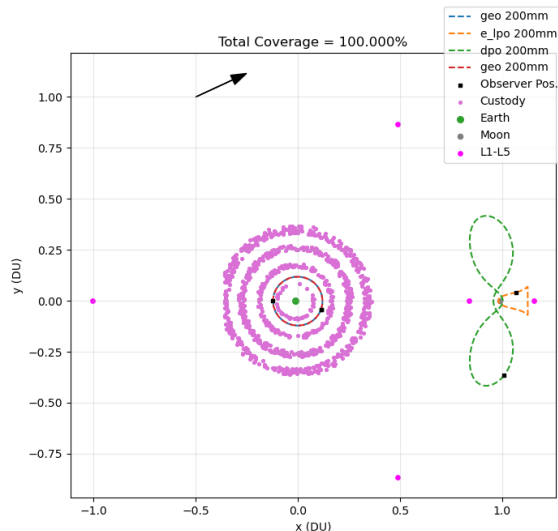
15
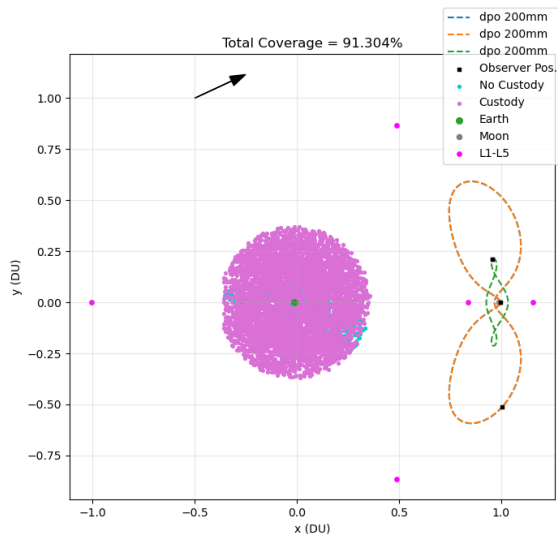
(a) Full 4xGEO Volume

(b) Clipped Volume

Figure 17: Total Coverage of Full Volume vs. Clipped Volume with 3 Observers

(a) Full 4xGEO Volume

(b) Clipped Volume

Figure 18: Total Coverage of Full Volume vs. Clipped Volume with 4 Observers

Over 99% observability can be attained through the utilization of two observers for the clipped volume, whereas the full volume merely attains an observability of 85%. In the case of the clipped volume, the achievement of 100% observability necessitates only three observers, whereas the full volume fall behind by nearly 6%.

As anticipated, the Cislunar architectures designed for the clipped volume consistently exhibited a notably higher degree of observability when compared to their counterparts within the complete 4xGEO sphere, even when employing the same number of sensors. Conversely, the clipped volume necessitated fewer sensors to sustain a high level of observability in comparison to the requisites of the full 4xGEO volume. This outcome carries the dual advantage of curtailing processing demands, simplifying inter-sensor coordination, and consequently reducing the overall mission costs.

Future studies may involve conducting a more in-depth analysis of the capacity differences between the full and clipped

16

volumes. This research will build upon the preceding efforts from the current study [7].

4.5 Return to Poincaré Mapping

Sections 4.2 and 4.3 focused on using a Poincaré-like surface that molded itself around a specific GEO radius. Thus far, the focus has been on finding methods to constrain the search volumes for regions about NxGEO Earth intersections. This section will focus on generating a Poincaré Map, similar to Figure 7, using all of the same manifold information from the previous sections. Instead of looking at the final intersections, planes are defined as shown in Figure 9 at X=0.5 DU ($\sim$4.6xGEO) and X=0.81132 DU (7.5xGEO), such that crossings can be evaluated. These could be optimized in the future, but to get a rough idea of the impact, the first plane at X=0.5 was chosen to be just outside of the 4xGEO sphere and the second plane, X=0.81132 was chosen to be near the L_1 gateway. Instead of detecting intersections when entering/leaving the NxGEO sphere, the trajectories can instead be evaluated at these plane crossings. The same method defined in Section 4.1 will be used with the stopping condition being the intersection of those planes in either direction.
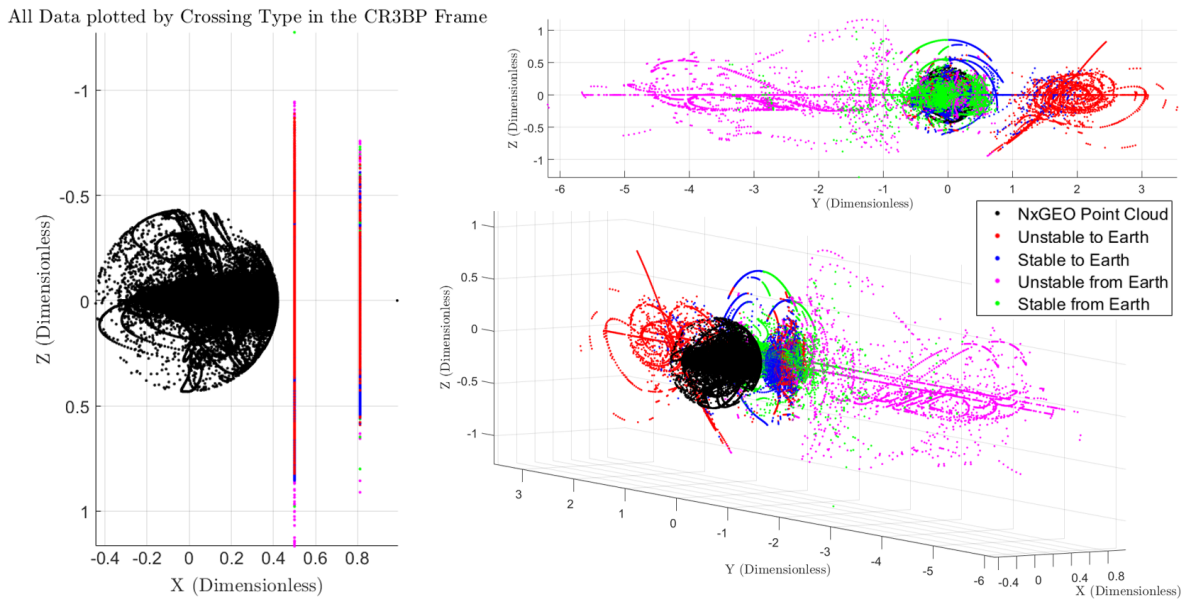

Figure 19: Various views of the Poincaré Maps and Poincaré-like surfaces

Figure 19 shows the original NxGEO point cloud in comparison to plane intersections. Immediately, the size of the Poincaré map dwarfs even the NxGEO sphere, which is plotted for scale here. With respect to the Z-axis, the height of the Poincaré map at the X=0.5 plane is twice as tall as the NxGEO sphere. The maps at X=0.5 and X=0.81132 contain random chaos (scattering of orbits), order (shapes), and has three unique areas. Along the Y-axis, cluster 1 stretches between -6 DU ($\sim$55.5xGEO) to -1 DU ($\sim$9.2xGEO), cluster 2 is centered between +/-1 DU ($\sim$9.2xGEO), and cluster 3 is bounded between 1 DU ($\sim$9.2xGEO) and 3 DU ($\sim$27.7xGEO). While cluster 1 and 3 are scientifically interesting as they postulate a well-defined integral of motion well outside the Earth-Moon system, monitoring those distances provide no strategic advantage and the solution space should be limited for the mission using this subset of periodic families and propagation criteria from section 4.1. Choosing an extent of the 10xGEO sphere results in a volume all the way out to almost L_2 to include the moon and L_1.

17

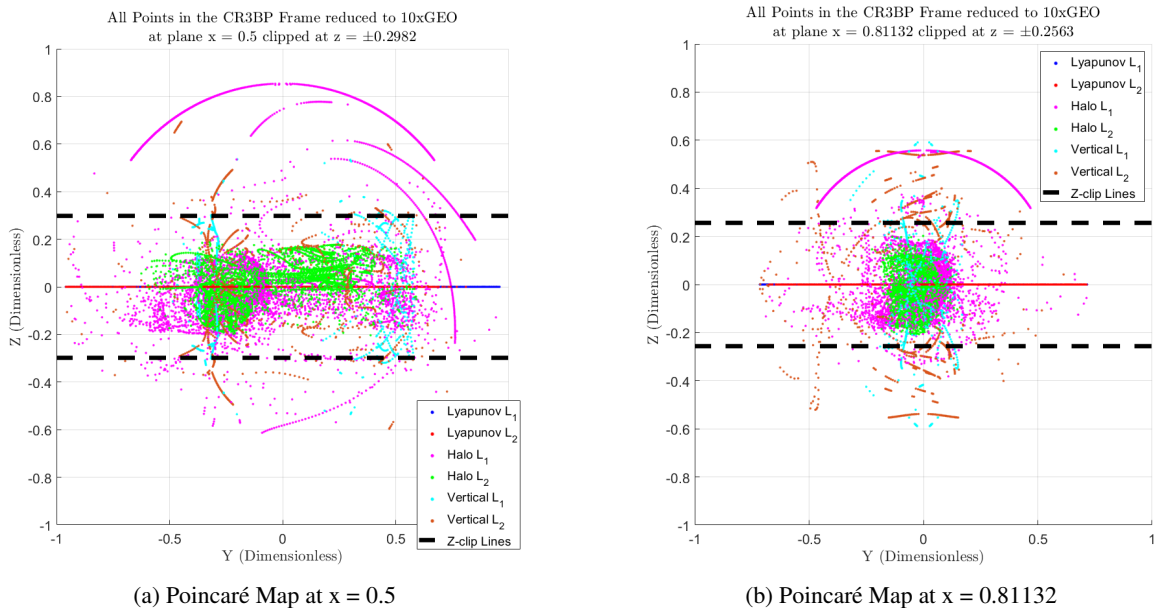(a) Poincaré Map at x = 0.5   (b) Poincaré Map at x = 0.81132

Figure 20: Poincaré maps reduced to fit within a 10xGEO Sphere

In Figure 20, the data was reduced to fall within the 10xGEO sphere. The data was further reduced by height in the Z-direction with the horizontal dashed lines that correspond to the average z-positions of each data set. Clusters 1 and 3 exist outside of the 10xGEO sphere and are not present in the GEO clipped data. The results for percentage of incoming and outgoing free-trajectory traffic an SDA mission observing the planes X=0.5 and X=0.81132 can see is shown in Table 7. It is important to note that some of the obvious curves seen, like the pink Halo L_1 are caused by the sheer size of the periodic orbit. The periodic orbits themselves actually intersect the surface of section, which leads to those obvious curves.

Table 7: Percentage of Free-Trajectory Traffic Discovered

Plane to Intersect	Stable	Unstable	Total
X=0.5 ($\approx$4.6xGEO)	88.90%	79.16%	84.19%
X=0.81132 (7.5xGEO)	84.37%	73.29%	78.67%

The Poincaré Maps provide an extremely useful tool for determining how to monitor the Cislunar and 10xGEO domains. Due to the physics of the manifolds, P_3 is bounded by deterministic avenues that can readily be observed. While this section only focused on a small set of manifolds between Earth, L_1 and L_2, this method can readily be used for all manifolds that traverse the Lagrange Points (L_1 through L_5) and any periodic orbit. For simplicity, this research used the simple definition of defining a final intersection surface that reduced all trajectories into trajectories of interest. Then using the trajectories of interest, planes were defined to create the Poincaré map. Both the initial surface and planes of intersections can be easily modified to generate Poincaré Maps at any location in space that an SDA mission could monitor.

5. CONCLUSIONS

In conclusion, this research has presented several methods for characterization and optimization techniques of these manifolds for SSA, SDA, and STM missions. It has been shown that it is possible to reduce the search volume utilizing the manifolds in the CR3BP to monitor free-trajectories, while still capturing more than 80% of the traffic. By defining a volume of interest, a subset of manifolds can be found that intersect that volume. Evaluating that subset of manifold trajectories results in clear patterns emerging which define bottlenecks that can be exploited. Using Poincaré-like surfaces and Poincaré maps enable volume reduction, resulting in a more optimized mission to reduce mission cost and complexity. Simple clipping techniques such as mean plus standard deviation clipping quickly reduces the searchable area while allowing approximately 80% coverage. Initial observability analysis reveals a significant reduction in the

number of observers needed to achieve complete coverage for the clipped volume in comparison to the full volume, thus reducing overall mission costs.

The Poincaré-like surfaces provide useful pattern analysis for tracking targets which could enter into a circular orbit about the Earth and Moon. More missions will have access to NxGEO and the Poincaré Maps provide a unique solution for tracking objects in a very large volume. While this paper focused on Lyapunov, Northern Halo, and Norther Vertical orbits, this method can be applied to any periodic orbit and its corresponding stable and unstable manifold. Future SDA missions are required to expand their capabilities and this paper offers solutions to how to monitor NxGEO spheres, the Cislunar Pathways, and missions around the Moon.

REFERENCES

[1] Klonowski, M., Holzinger, M. J., and Fahrner, N. O., "Optimal cislunar architecture design using monte carlo tree search methods," *The Journal of the Astronautical Sciences* **70**(3), 17 (2023).

[2] Poincaré, H., "Sur les courbes définies par les équations différentielles," *Journal de Mathématiques Pures et Appliquées* **7**(2), 375–420 (1912).

[3] Conley, C. C., "Low energy transit orbits in the restricted three-body problem," *SIAM Journal on Applied Mathematics* **16**(4), 732–746 (1968).

[4] NASA, "Three body periodic orbits," *https://ssd.jpl.nasa.gov/tools/periodic_orbits.html/intro* (2023).

[5] Escribano, T. M. V., "Poincare sections and resonant orbits in the restricted three-body problem," *Purdue Master of Science Thesis* (2010).

[6] Barden, B. T., Howell, K. C., Lo, M. W., and Miller, J. K., "Application of dynamical systems theory to trajectory design for a libration point mission," *Journal of The Astronautical Sciences* **45**, 161–178 (1997).

[7] Fahrner, N. O., "Capacity-based cislunar space domain awareness architecture optimization," *AMOS* (2022).